# Induced magnetism on silicon in $Fe_3Si$ quasi-Heusler compound

C. Antoniak,[1] H. C. Herper,[1] Y. N. Zhang,[2] A. Warland,[1] T. Kachel,[3] F. Stromberg,[1] B. Krumme,[1] C. Weis,[1] K. Fauth,[4] W. Keune,[1] P. Entel,[1] R. Q. Wu,[2] J. Lindner,[1] and H. Wende[1]

[1]*Fakultät für Physik and Center for Nanointegration Duisburg-Essen (CeNIDE), Universität Duisburg-Essen, Lotharstr. 1, 47048 Duisburg, Germany*

[2]*Department of Physics and Astronomy, University of California, Irvine, California 92697, USA*

[3]*Helmholtz-Zentrum Berlin für Materialien und Energie – Speicherring BESSYII, Albert-Einstein-Str. 15, 12489 Berlin, Germany*

[4]*Experimentelle Physik IV, Universität Würzburg, Am Hubland, 97074 Würzburg, Germany*

(Received 6 October 2010; published 26 June 2012)

Element-specific magnetic moments of epitaxially grown $Fe_3Si$ in $D0_3$ crystal symmetry were analyzed by means of x-ray absorption spectroscopy and its associated magnetic circular dichroism. To detect the weak magnetization induced at the Si sites, measurements were performed at both the Si $K$ edge and the Si $L_{3,2}$ edges. By band structure calculations based on either the SPR-KKR method or FLAPW with GGA, the spectroscopic features could be reproduced and provide an insight to the underlying physics. In addition, comparison of the experimental data to calculated spectra made it possible for us to estimate the induced effective spin and orbital magnetic moment of Si in our sample, i.e., $\mu_s^{\text{eff}} = (-0.011 \pm 0.005)\ \mu_B$ and $\mu_l = (-0.003 \pm 0.003)\ \mu_B$, respectively. The sign and the order of magnitude of the tiny orbital magnetic moment has been confirmed by application of the magneto-optical sum rule.

DOI: 10.1103/PhysRevB.85.214432 PACS number(s): 75.50.Bb, 78.70.Dm

## I. INTRODUCTION

In spintronics or magnetoelectronics, the intrinsic spin of an electron and its associated magnetic moment is used as a carrier for information in addition to its electronic charge. Compared to devices based on conventional charge transport, spintronic devices offer the possibility to realize fast processing at low power costs. The spin-polarized current needed in this case can be generated by passing the current through a ferromagnetic electrode. In order to combine this new field of electronics with the established semiconductor technologies, spin injection from the ferromagnet into a semiconductor is essential and has already been extensively investigated.[1–3] The $Fe_3Si$ compound on GaAs has turned out to be a promising candidate of ferromagnet/semiconductor systems with its spin injection efficiency of above 2% at a temperature of 150 K and 1% at room temperature.[4]

$Fe_3Si$ is a quasi-Heusler compound that crystallizes in the $D0_3$ symmetry in the chemically ordered phase with a lattice constant $a = 5.65$ Å. As depicted in Fig. 1, Fe atoms are located at two inequivalent lattice sites (A and B), and Si occupies the lattice site C. While Fe-A atoms are surrounded by four Fe and four Si nearest neighbor atoms, Fe-B atoms are surrounded by eight Fe nearest neighbor atoms. Random occupancies of sites B and C, or all three sites, lead to a B2 (CsCl)-like or A2 (bcc) symmetry, respectively. Due to the different neighborhood in the $D0_3$ structure, Fe-A and Fe-B atoms have different magnetic moments, namely 1.2 $\mu_B$ and 2.4 $\mu_B$ as obtained from neutron diffraction experiments.[5] The structure of $Fe_3Si$ can be represented by the long-range ordering parameters S(B2) and S($D0_3$) which are defined by the occupation probabilities $P_i$ of Fe at the different lattice sites $i$ = A, B by the following equations:[6]

$$\mathrm{S(B2)} = \frac{1}{2}\,\frac{P_A - (1-x)}{x(1-x)} \tag{1}$$

$$\mathrm{S(D0_3)} = \frac{1}{4}\,\frac{2P_A + P_B - 3(1-x)}{x(1-x)}, \tag{2}$$

where $x$ denotes the Si content, i.e., $x = 0.25$ in the case of $Fe_3Si$. A perfect $D0_3$ structure is described by S($D0_3$) = 1 and S(B2) = 2/3, respectively. When grown onto a semiconductor like GaAs, the actual crystal symmetry should be strongly disturbed by interfacial diffusion[7] which influences the electronic and magnetic properties as well.[8] To avoid diffusion of Ga and/or As atoms into the metal, a tunnel-barrier spin-injector was used in this work, i.e., $Fe_3Si$ was grown on 3 nm MgO on GaAs(001). For this case, the magnetic properties can be well controlled at the interface, which is more stable even at elevated temperatures than direct ferromagnet/semiconductor heterostructures. In addition, increasing the interface resistance by a MgO tunnel barrier helps to reduce the large impedance mismatch[9] that prevents efficient spin injection across the interface.

A lot of effort has been made over the last decades to characterize $Fe_3Si$ compounds in terms of phase stability, structure, electronic and magnetic properties.[10,11] However, its static and dynamic magnetization behavior is strongly dominated by Fe due to its large magnetic moment with respect to Si and three times larger amount. Therefore, a direct measurement of the weak magnetization of Si—necessary for the complete understanding of the magnetic properties of the compound—has remained a challenge for years. In this paper, we focus on the induced magnetism on Si: By measuring the x-ray absorption near-edge structure (XANES) and x-ray magnetic circular dichroism (XMCD) not only at the Fe $L_{3,2}$ absorption edges, but also at the Si $L_{3,2}$ and Si K edges, a clear evidence of a magnetic signal from Si was found. By comparison with spectra obtained from band structure calculations using the Korringa-Kohn-Rostoker (KKR) method on the one hand and the full potential linearized augmented planewave (FLAPW) approach on the other hand, we reached quantitative understanding of structural and magnetic properties.

The organization of the paper is as follows: In Sec. II, Mössbauer spectroscopy is introduced to structurally

 

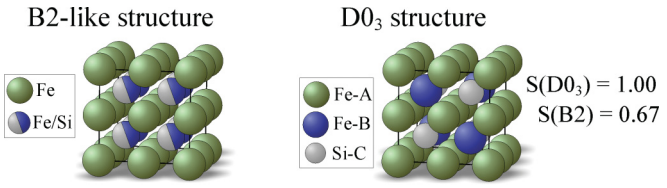


FIG. 1. (Color online) Schematic B2-like and $D0_3$ structure of $Fe_3Si$.

characterize the $Fe_3Si$ system by extracting the long-range ordering parameters $S(D0_3)$ and S(B2), respectively, before we turn to the XANES and XMCD measurements. In Sec. III we present the details of band structure calculations using the two methods mentioned above. The induced magnetism of Si in $Fe_3Si$ is discussed in Sec. IV by comparison of experimental and calculated spectra before conclusions are given in the last section.

## II. EXPERIMENTAL

### A. Performance and sample characterization

To preserve the chemical ordering, a tunnel-barrier spin-injector was used in this work. After growing 3 nm MgO on cleaned GaAs(001) with a $(4 \times 6)$ surface reconstruction, two samples of 8 nm $Fe_3Si$ were prepared by coevaporation of Fe and Si in a UHV chamber with a base pressure of $10^{-8}$ Pa. They were grown at a substrate temperature of 250 °C with deposition rates of 0.064 Å/s of $^{57}$Fe and 0.036 Å/s of Si, respectively. One sample was subsequently annealed at 500 °C before capping with 3 nm MgO to prevent oxidation of the $Fe_3Si$ film. Conversion electron Mössbauer spectroscopy (CEMS) at perpendicular incidence of the $\gamma$ rays onto the film surface was employed to investigate the degree of $D0_3$ order of the two samples.

The experimental CEMS data can be fitted by the procedure described by Arita *et al.*,[6] yielding the long-range ordering parameters $S(D0_3)$ and S(B2). The samples prepared here obviously display a high degree of chemical and structural order as can be seen from the Mössbauer results shown in Fig. 2. For the nonannealed sample we found $S(D0_3) = 0.86$ and $S(B2) = 0.53$, respectively. Annealing of the sample leads to an even higher degree of chemical order as indicated by the ordering parameters $S(D0_3) = 0.88$, $S(B2) = 0.55$.

X-ray absorption measurements were performed at the PM-3 bending magnet beamline at the HZB-BESSY II synchrotron radiation facility in Berlin/Germany at $T = 14$ K in magnetic fields of $\mu_0 H_{\text{ext}} = \pm 1$ T in total electron yield (TEY) mode by measuring the sample drain current. The SX700-type plane grating monochromator (PGM) offers the possibility to measure at variable degree of circular polarization $\sigma$ in the energy range between 20 eV and about 2000 eV with an energy resolution in the order of $10^{-3}$–$10^{-4}$. Here, the photon energy was varied between 90 eV $\leqslant E \leqslant$ 130 eV around the Si $L_{3,2}$ absorption edges, 680 eV $\leqslant E \leqslant$ 790 eV around the Fe $L_{3,2}$ edges, and 1820 eV $\leqslant E \leqslant$1960 eV around the Si K edge. For all cases, the fixed focus constant was set to the standard value $c_{ff} = 2.25$. With the specific settings actually used in our experiment, the absolute values of energy resolution were estimated to be 15 meV at 100 eV and 1.24 eV at 1850 eV, respectively.

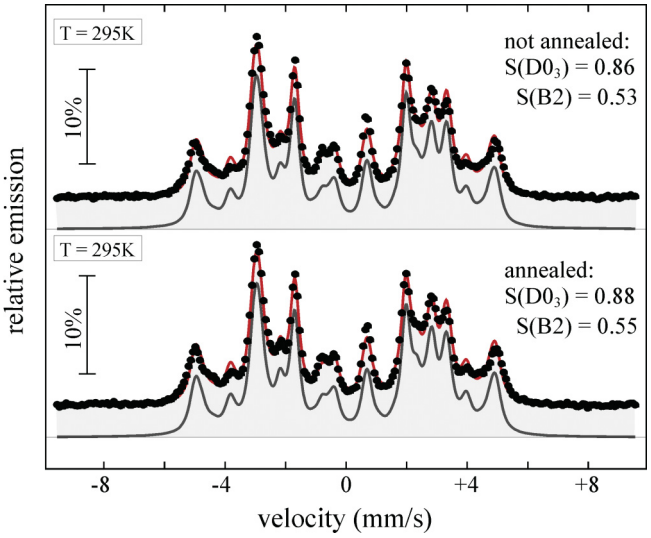


FIG. 2. (Color online) Conversion electron Mössbauer data of nonannealed (upper panel) and annealed (lower panel) $Fe_3Si$ at room temperature and fitted spectra with the extracted long-range ordering parameters $S(D0_3)$ and S(B2). Note that a perfect $D0_3$ symmetry is represented by $S(D0_3) = 1$ and $S(B2) = 2/3$.

In order to optimize the experimental figure of merit—containing $\sigma^2$ times the photon flux—different out-of-plane (vertical) angles of the emitted x-rays with respect to the storage ring plane had to be used for the various photon energies. The different resulting values of $\sigma$ were calculated for the energy of Si $L_{3,2}$, Si K, and Fe $L_3$ absorption edges using the well-known equations for the emission characteristics of the radiation.[12] At the Fe $L_3$ edge the calculated values were checked by measuring the asymmetry of an Fe bulk sample for different monochromator settings, i.e., for x-rays emitted under different vertical angles. For the actual settings used we found $\sigma = 92.5\%$ for measurements at the Fe $L_{3,2}$ absorption edges, $\sigma = 76.5\%$ at the Si K edge, and $\sigma = 88.0\%$ at the Si $L_{3,2}$ absorption edges.

After each scan, either the magnetic field or the photon helicity was reversed. Field-dependent magnetization curves were measured at the photon energy of 710 eV at the Fe $L_3$ edge normalized to the pre-edge signal at 700 eV and at the Si K edge at a photon energy of 1851 eV normalized to the pre-edge signal at 1841 eV.

For XANES and XMCD data analysis, a linear background was subtracted from the experimental data. In the case of Fe, electron excitations into the final $3d$ states were separated from the ones into higher states or the continuum by a two steplike function necessary for the determination of spin and orbital magnetic moments by a standard sum rule-based analysis.[13–15] Since this procedure fails in the case of Si due to its broad $p$ band, spin and orbital magnetic moments of Si were estimated by comparison to calculated spectra. Only the sign and the order of magnitude could reliably be estimated by application of the sum rule for XMCD at the K edge.[16,17] The intra-atomic dipole term $\mu_t$ that is included in the experimentally obtained effective spin magnetic moment $\mu_s^{\text{eff}} = \mu_s + 7\mu_t$ is assumed to be negligible in the cubic $Fe_3Si$ system investigated in this

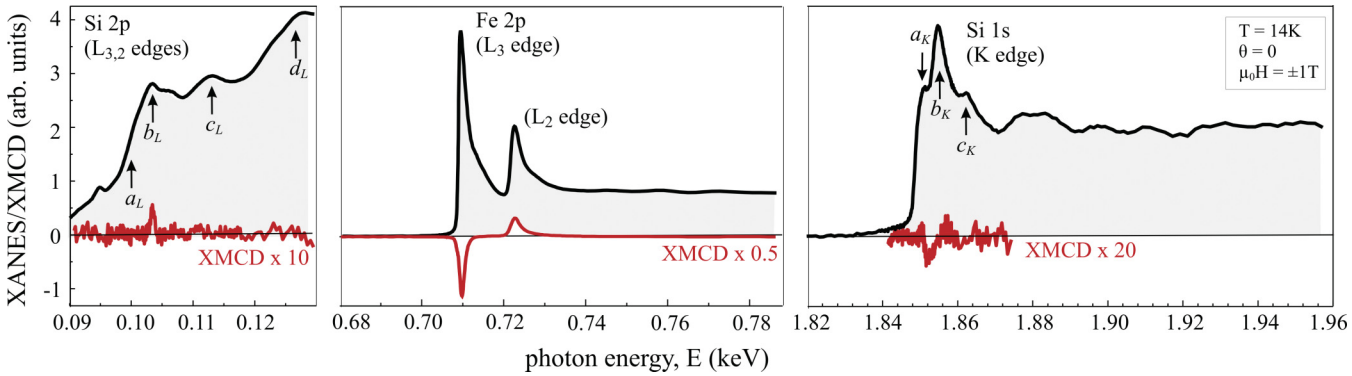


FIG. 3. (Color online) X-ray absorption near-edge structure and circular dichroism at Si $L_{3,2}$, Fe $L_{3,2}$, and Si K absorption edges of annealed $Fe_3Si$ measured at $T = 14$ K under normal x-ray incidence. The external magnetic field was applied parallel to the x-ray beam.

work. However, since $\mu_t$ is probably not vanishing completely, the spin magnetic moments derived from experimental data are denoted *effective* spin magnetic moment.

### B. Results

Experimental x-ray absorption spectra of Fe and Si in $Fe_3Si$ are shown in Fig. 3. In the case of Fe, the spectra are already corrected for self-absorption and saturation effects[18] assuming an electron escape depth of $\lambda_e = 2$ nm. Similar to the CEMS data, no significant difference between the annealed and nonannealed sample is observed. Thus, we focus here on the annealed sample which exhibits a slightly improved chemical ordering. At the Fe $L_{3,2}$ absorption edges, the spectral shape of XANES and its associated XMCD indicate an Fe-*d*/Si-*sp* hybridization of Fe on lattice sites A (cf. Fig. 6) as discussed in the literature on the basis of calculated spin and angular momentum resolved density of states.[8]

In the case of Si, the $L_3$ and $L_2$ edges are not energetically well separated. There are six spectral features visible in the XANES shown in Fig. 3. Four of them, $a_L, b_L, c_L$, and $d_L$, arise from Si in $Fe_3Si$ as will be revealed later by comparison with calculated spectra. (The index $L$ is related to the absorption edge.) The small pre-edge peak at 95 eV can be assigned to Mg of the MgO cap layer. An additional shoulder in the experimental XANES above $b_L$ (around 107 eV) may be an indication for a Si-rich interface to the MgO cap layer since Si tends to segregate at the surface of Fe-Si alloys. The XMCD signal at the Si $L_{3,2}$ absorption edges shows a maximum asymmetry of only about 0.8% and is enlarged by a factor of 10 in Fig. 3 for clarity. In order to ensure the reliability of the XMCD signal, not only pairs of spectra with reversed sample magnetization but also with different polarization of x-rays were analyzed. Interestingly, a meaningful XMCD can only be found around 104 eV, the position of the peak $b_L$. Compared to the Fe signal at the $L_3$ absorption edge, the reversed sign of the XMCD at the Si sites already suggests an antiparallel alignment of Fe and Si spins.

The XMCD at the K edge is sensitive only to the orbital magnetic contribution which is known to be very small. Nevertheless, in our experiment a clear magnetic signal was measured with a maximum XMCD asymmetry of about 0.3%. Although this value of asymmetry is extremely small, we were able to directly measure the field-dependent magnetization by detecting the absorption signal at the energy position of the maximum XMCD signal, i.e., 1851 eV, while sweeping the external magnetic field.[19] The signal was normalized to the pre-edge signal at 1841 eV. Equivalent measurements were performed at the Fe $L_3$ edge at photon energies of 710 and 700 eV, respectively. The results are shown in Fig. 4. Although it is almost at the detection limit, it can clearly be seen that the field dependence of the Si XMCD follows the one measured at the Fe sites. A magnetic hysteresis could not be measured since the superconducting magnet used in this experiment is not well suited to resolve small coercive fields.

## III. *AB INITIO* CALCULATIONS

### A. Computational details

In order to provide insight for the explanation of experimental data, the XANES and XMCD spectra of bulk $Fe_3Si$ were calculated using density functional approaches. The optical absorption tensor was calculated by means of the linear response formula proposed by Wang and Callaway.[20] While the calculated XANES and XMCD spectra at the Fe $L_{3,2}$ absorption edges match well the measured data,[8] the reliability of calculations at the Si edges is unclear due to the delocalized nature of its $3p$ states. In particular, the influence of muffin tin (MT) approximation on the quality of spectra is not known at the present. Here we use two different methods, namely the spin polarized relativistic KKR (SPR-KKR) technique[21]

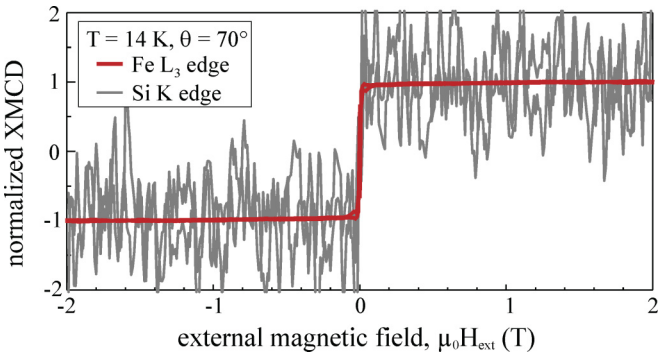


FIG. 4. (Color online) Element-specific field dependent magnetization measured by means of XMCD at the Fe $L_3$ edge (710 eV) and Si K edge (1851 eV), respectively.

and the full-potential linear augmented plane wave (FLAPW) method, for the determination of magnetic properties of $Fe_3Si$. Using these two methods also gives the possibility to ensure that the results do not significantly depend on the approximations made in the electronic structure calculations, namely the atomic sphere approximation (ASA) or non-fully-relativistic treatment.

Within the SPR-KKR method the electronic structure is represented in terms of Green's functions evaluated by means of the multiple scattering theory. The ASA is adopted and the interstitial region is eliminated by using overlapping spheres. In contrast, the FLAPW is viewed as the most precise approach with no shape approximation in the entire space for wave function, charge density, and potential.[22,23] The core electrons were described fully-relativistic, while the valence electrons are treated in a scalar-relativistic manner, and the spin-orbit coupling term for the valence states was invoked second variationally.[24] In both SPR-KKR and FLAPW calculations we used the generalized gradient approximation (GGA) in the parametrization of Perdew, Burke, and Ernzerhof[25,26] to describe the exchange correlation interaction. The lattice constant of the $D0_3$ unit cell was chosen based on experimental data, $a = 5.65$ Å. Integrations over the Brillouin zone (BZ) were evaluated over a $20 \times 20 \times 20$ $k$-point grid. The convergence against energy cutoffs and the maximum angular momentum $l_{\max}$ were carefully monitored. In the SPR-KKR calculations $l_{\max} = 3$ was used for the calculation of the spectra, whereas $l_{\max} = 8$ was used in the FLAPW calculations.

### B. Results

The magnetic moments obtained from the *ab initio* calculations are summarized in Table I. Obviously the spin moments $\mu_s$ at the Fe sites are overestimated by both methods. It has been noted in many theoretical studies[27–29] that for the transition metals, in particular the $3d$ metals, the GGA always produce larger lattice parameters and smaller bulk moduli compared with the local spin density approximation (LSDA) results. It was also pointed out by Singh and Ashkenazi[30] that in GGA there is an increased tendency towards magnetism in general, and particularly towards larger magnetic energies for magnetic materials, which in other cases may just result in a small quantitative error. Furthermore, discrepancies between the magnetic moments obtained from FLAPW and SPR-KKR are mainly dedicated to the choice of the Wigner Seitz sphere used for the projection to the lattice.

XANES and XMCD spectra at the Si $L_{3,2}$ and K edges as well as the Fe $L_{3,2}$ edges calculated by means of SPR-KKR and FLAPW method, respectively, are shown in Fig. 5. The nicely reproduced main features of the experimental XANES and XMCD indicate the validity of our computational approaches and parametrizations. The $D0_3$ structure assumed in our calculations should be rather dominant in the measured samples. As evidence for the insignificance of ASA, the spectroscopic profiles obtained from the SPR-KKR and FLAPW methods closely follow each other in the entire energy range. This can be understood since the x-ray spectra depend on the overlap between valence and atomic-like core states. The two peaks at 95 and 107 eV arise from the MgO buffer layer and possible deviations from the $Fe_3Si$ composition at the film surface and hence are missing in the theoretical data. As in the experiment, the Si $L_{3,2}$ XANES spectrum exhibit an onset peak at the photon energy of about 97 eV followed by three pronounced peaks at 104, 110, and 121 eV denoted as $a_L$, $b_L$, $c_L$, and $d_L$ as in Fig. 3. The XMCD spectrum only shows an intense positive peak at $b_L$ in good accordance with the experimental data. The amplitudes of the XMCD at the Si absorption edges appears to be very weak at both the $L_{3,2}$ and K edges (less than 1% of the XANES). This indicates that the induced spin and orbital magnetic moments on Si are small (cf. Table I).

TABLE I. Site-specific spin and orbital magnetic moments of Fe and Si in $Fe_3Si$ calculated by SPR-KKR and FLAPW.

| | Fe A sites | | Fe B sites | | Si C sites | |
|---|---|---|---|---|---|---|
| method | KKR | FLAPW | KKR | FLAPW | KKR | FLAPW |
| $\mu_s$ [$\mu_B$] | 1.39 | 1.33 | 2.67 | 2.55 | −0.121 | −0.062 |
| $\mu_l$ [$\mu_B$] | 0.030 | 0.020 | 0.054 | 0.051 | −0.0019 | −0.0004 |

Since both XANES and XMCD signals are related to the dipole transitions from the inner-shell states to the unoccupied valence states,[31,32] it is useful to analyze the density of states (DOS) above the Fermi level $E_F$. Here, the partial DOS curves of $Fe_3Si$ obtained from the FLAPW are presented in Fig. 6. As discussed in the literature,[8,33] the two types of Fe atoms have different electronic properties, and the Fe-A atoms have a strong effect on the DOS profiles of Si atoms. Interestingly, there are two pronounced peaks in the Si s-DOS curves at about 5 eV above $E_F$, slightly split in two spin channels. They reflect the hybridization between the $t_{2g}$ orbitals of Fe-A atoms and the Si $s$ states. Via intra-atomic hybridization, this feature can also be found in the $d$ DOS and result in the peaks in the Si $L_{3,2}$ XMCD curves at 104 eV. (For an easier assignment, this region is denoted as $b$ in the DOS since it is related to the spectral features of XANES and XMCD denoted $b_L$, $b_K$ in Fig. 5.) The K edge involves electronic excitations from the $1s$ core states towards the $p$ conduction states. These states mediate the magnetization in $Fe_3Si$ and are the main ingredients in the valence and conduction bands of this alloy. Figure 6 shows that the contribution to the positive onset at the Si K edge XMCD is ascribed to the $p$ state above $E_F$ in the majority spin channel. The pronounced resonant peaks for Si, Fe-A, and Fe-B atoms in 1–2 eV (denoted $a$) are responsible for the large negative peak of the XMCD spectra at the Si K edge (denoted $a_K$).

## IV. DISCUSSION

The results of XANES and XMCD spectra plotted in Fig. 7 display that the density functional calculations using the perfect $D0_3$ structure reproduce very well the experimental data, in particular the XMCD. It is well known[33–35] that XMCD spectra of dia- or paramagnetic elements with induced ferromagnetism in an alloy can be utilized to characterize atomic arrangements since their spectroscopic features are highly sensitive to the change in interactions with ferromagnetic species. It is reasonable to conclude that the $Fe_3Si$ films used in the experiment consist mainly of $D0_3$ symmetry. In addition, the good agreement between theory and experiment in the XMCD features indicates the possibility of determining tiny magnetic moments in complex compounds.

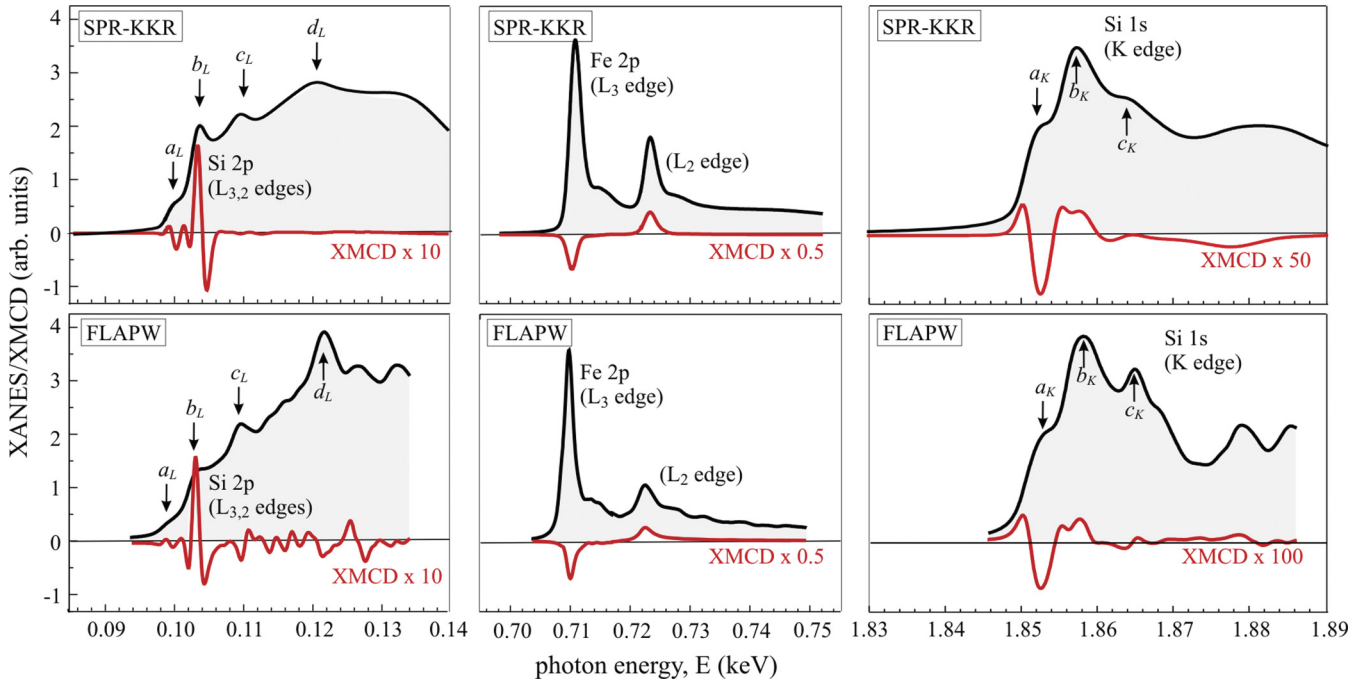


FIG. 5. (Color online) Calculated XANES and XMCD spectra at the Si $L_{3,2}$, $Fe_{3,2}$ and Si K edges by means of SPR-KKR (upper panel) and FLAPW (lower panel), respectively.

Taking a closer look at the XANES and XMCD signals, the agreement of the Si XANES is less satisfactory compared to the XMCD. Since we only considered the initial state effect in the optical transition, we do not attempt to go much beyond the comparison on peak positions. Furthermore, the FLAPW method produced more fine structures in the higher energy range compared to the SPR-KKR results. This discrepancy can be assigned to the fact that the SPR-KKR method uses Wigner-Seitz partition for the whole space, thus eliminating the interstitial region from the formalism.[27,36]

The effective spin and orbital magnetic moments at the Fe sites were determined by a sum-rule based analysis of the XMCD and are listed in Table II. Note that it is impossible to distinguish between the moments of Fe on lattice sites A and B through analyzing the absorption spectra at the $L_{3,2}$ edges since the differences in energy position and spectral shape are marginal. The averaged Fe moment is significantly smaller than in bulk $\alpha$-Fe and in good agreement to values reported earlier.[8] For a better comparison with our calculations, the magnetic moments obtained from theory were also site averaged and listed in Table II.

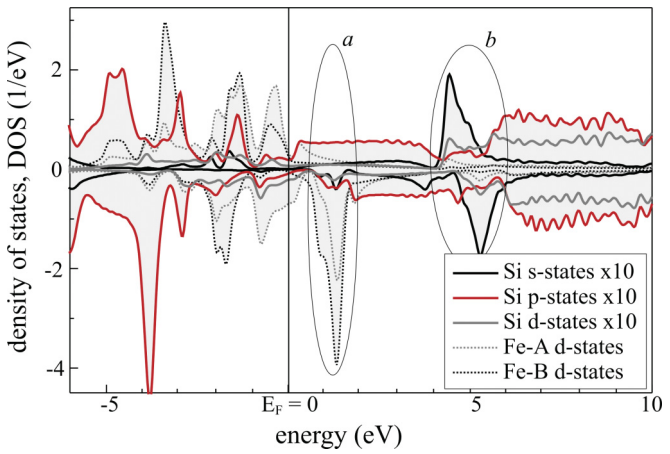


FIG. 6. (Color online) The spin and orbital resolved density of states of $Fe_3Si$. Positive and negative sides are for the spin-up and spin-down parts, respectively. The amplitude for Si *s*-, *p*-, and *d*-states are rescaled by a factor of 10.

The intrinsic and instrumental broadening of the experimental spectra yield a strong overlap of the $L_3$ and $L_2$ edges of Si. Also the FLAPW calculation shows that the energy separation between $2p_{1/2}$ and $2p_{3/2}$ states is only 0.6 eV. Thus, a straight-forward determination of spin and orbital magnetic moments by integral methods is impossible.[37] Nevertheless, the good agreement between theory and experiment allows us to access this information from theory with confidence. To better appreciate the quality of our results, the experimental Si XMCD signal at both $L_{3,2}$ and K edges are rescaled and compared in Fig. 7. The magnetic moments in our sample can be estimated by comparing the scaling factors of XANES and XMCD. This procedure is commonly used for experimental data for which the standard sum-rule based analysis fails.

At the Si K edge, the experimental XANES was scaled by a constant factor to fit the intensity of the corresponding spectrum calculated by the SPR-KKR method in the pre- and post-edge region. Note that the spectra shown in Fig. 7 correspond to the absorption cross-section in units of Mb ($1\ \mathrm{b} = 10^{-28}\ \mathrm{m}^2$) and no longer in arbitrary units. However, scaling the XMCD with the same factor is not sufficient to achieve good agreement between experimentally and theoretically obtained dichroism. At the Si $L_{3,2}$ edges, the experimental XMCD spectrum had to be enlarged by a factor

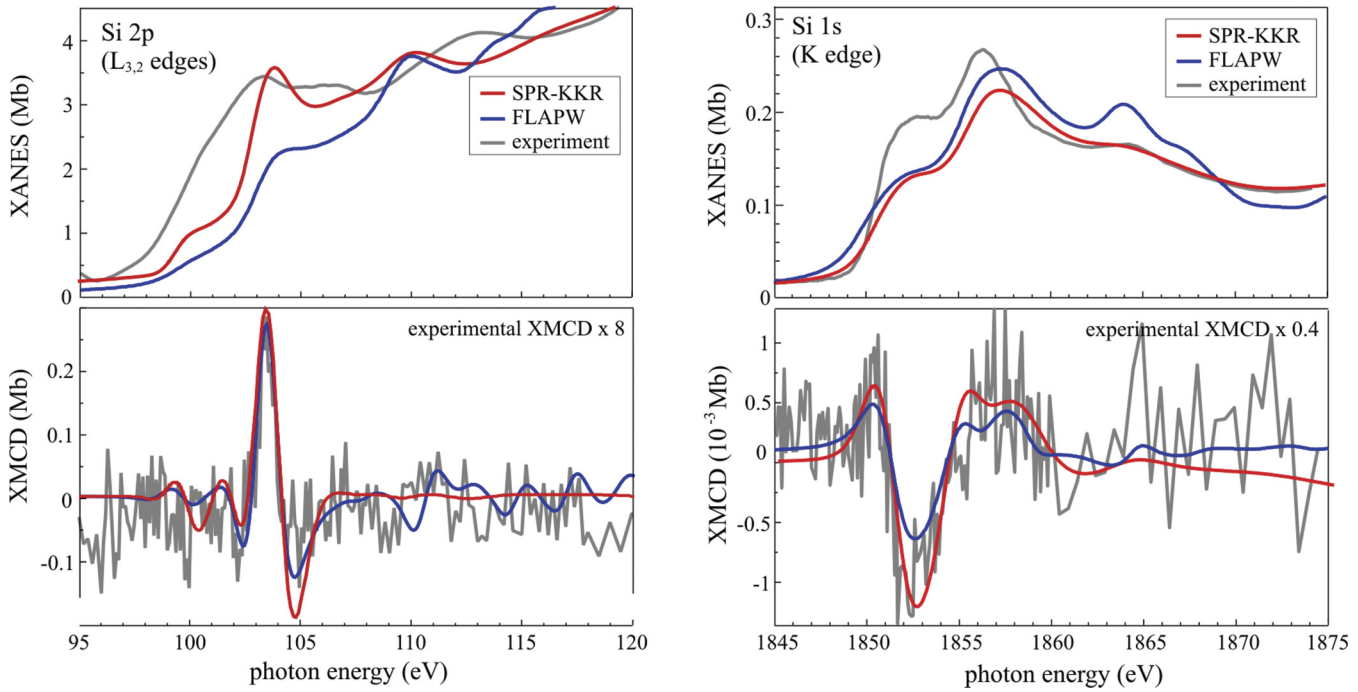


FIG. 7. (Color online) Experimentally obtained and calculated XANES and XMCD at the Si $L_{3,2}$ absorption edges and the Si K edge, respectively. The experimental data were normalized to fit the calculated XANES intensity in the pre- and post-edge region. To fit the intensity of the calculated dichroism, experimental XMCD data have been scaled by an additional factor that is used for an estimation of the magnetic moments of Si in the $Fe_3Si$ sample.

of about 6 in order to coincide with the calculated one. Since the major contribution to the XMCD asymmetry arises from the spin magnetic moment in this case, it can be concluded that the spin magnetic moment at the Si atoms in our sample is roughly eight times smaller than the theoretically expected value, i.e., $\mu_s^{\text{eff}} = (-0.011 \pm 0.005)\ \mu_B$. At the Si K edge, the experimental XMCD signal is sensitive only to the orbital magnetic moment and has to be scaled down by a factor of 0.4 to be in good agreement with the calculated spectrum. Consequently, the orbital magnetic moment in our sample is about twice as large as the theoretically expected value, i.e., $\mu_l = (-0.003 \pm 0.003)\ \mu_B$. The large error bar arises not only from the low signal-to-noise ratio of the experimental data, but also from the difference in calculated magnetic moments by the two different methods, although the amplitude of XMCD is roughly the same.

TABLE II. Site-averaged (effective) spin and orbital magnetic moments of Fe and Si in $Fe_3Si$ determined by XMCD and band structure calculations by two different approaches. Note that the effective spin magnetic moment $\mu_s^{\text{eff}}$ extracted from experimental data is denoted $\mu_s$ for an easier reading of the table.

| Fe | $\mu_s$ [$\mu_B$] | $\mu_l$ [$\mu_B$] |
|---|---|---|
| experiment | $1.76 \pm 0.10$ | $0.073 \pm 0.01$ |
| KKR | 1.82 | 0.038 |
| FLAPW | 1.73 | 0.030 |
| **Si** | $\mu_s$ [$\mu_B$] | $\mu_l$ [$\mu_B$] |
| experiment | $-0.011 \pm 0.005$ | $-0.003 \pm 0.003$ |
| KKR | $-0.121$ | $-0.0019$ |
| FLAPW | $-0.062$ | $-0.0004$ |

For the sake of completeness, the magneto-optical sum rule has been applied to the data obtained at the Si K edges as presented below. However, since the energy cutoff for the integral and hence the number of $p$ holes are not well defined for the itinerant $p$ states, one should keep in mind that the validity of this analysis is questionable in our case. Following the magneto-optical sum rule for the K edge as derived by Igarashi and Hirai,[16,17] the orbital magnetic moment can be calculated according to

$$\mu_l^p = \frac{2}{3} n_h^p \frac{\int_K \mu_c(E) dE}{\int_K \mu_0(E) dE}, \tag{3}$$

where $\mu_c = \mu_+ - \mu_-$ is the XMCD signal and $\mu_0 = \mu_+ + \mu_-$ is the so-called white line intensity of the XANES. The latter is shown in Fig. 8 after subtraction of a steplike background together with the integrals of the white line and XMCD respectively are shown in Fig. 8 for the experimental data and the spectra calculated by the SPR-KKR method. Using a rough estimation for the number of unoccupied $p$ states, $n_h^p = 3$, we obtain for the calculated spectra an orbital magnetic moment of about $\mu_l \approx -0.0015\ \mu_B$ in agreement with the value obtained directly by this calculation. However, it can be seen in Fig. 8 that the value depends on the cutoff energy for the integrals. For the case of the experimental data, the value of $\mu_l$ depends even stronger on the cutoff energy. The strong oscillations of the XMCD signal and, consequently, in the integral of the XMCD may be related to the magnetic counterpart of the extended x-ray absorption fine

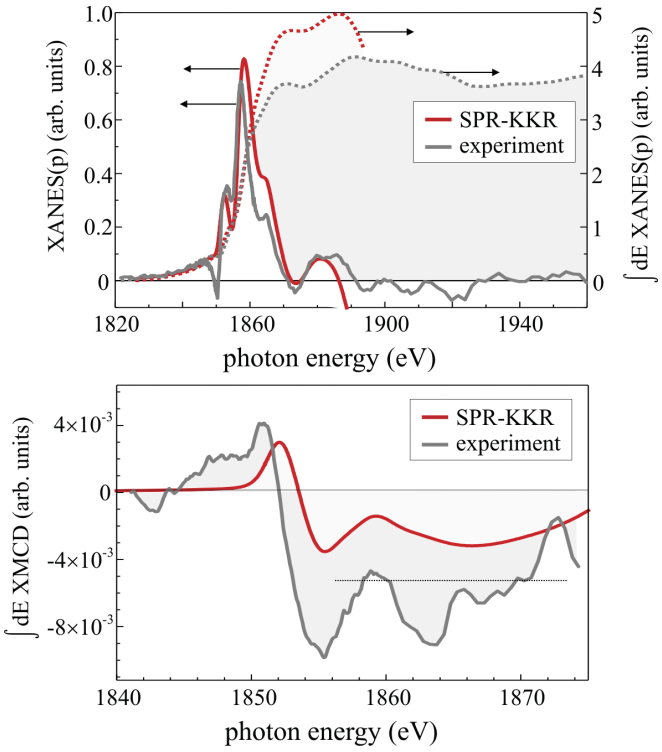


FIG. 8. (Color online) XANES after subtraction of steplike background for experimental data (gray line) and SPR-KKR calculation (red line), respectively, and their integrals (top). Integral of XMCD signal of experimental data and SPR-KKR calculation (bottom).

structure (MEXAFS). While the extended x-ray absorption fine structure (EXAFS) is an interference effect between the outgoing photoelectron as a matter wave and backscattered waves from neighboring atoms, MEXAFS includes a spin dependence of the scattering events.[37] In our case, the Si atoms are surrounded by Fe atoms with a quite large magnetic moment. Thus, the MEXAFS is expected to give a quite large contribution to our magnetic signal with respect to the small XMCD of Si with its tiny magnetic moment, and the integral value of the Si XMCD can only be estimated. Here, we choose the value by averaging the signal above 1862 eV as depicted by a horizontal line in Fig. 8. With this method the orbital magnetic moment amounts to $\mu_l \approx -0.003\mu_B$ which is in agreement with the value presented above obtained by scaling the experimental data to fit the calculated spectra. Although the absolute value from the sum-rule-based analysis is ambiguous, the negative sign of $\mu_l$ can be confirmed. In addition, it is obvious that the integral of the XMCD (Fig. 8), and consequently the orbital magnetic moment, is larger in the experiment than in the SPR-KKR calculation.

In the following, we turn to the discussion of some reasons for the different spin and orbital magnetic moments in theory and experiment. The spin magnetic moments at the Si sites may be reduced by a nonperfect surface of the $Fe_3Si$ film: As already mentioned above, the shoulder in the XANES above the Si $L_{3,2}$ absorption edge may indicate a segregation of Si at the $Fe_3Si$ surface which likely occurs in Fe-Si alloys and alters the composition ratio and atomic structure. This is reported in the literature,[38] where the cubic FeSi (c-FeSi) was found to influence the spectral shape of photoemission spectra[39] of $Fe_3Si$ a few eV above the main absorption edge similar to our experimental findings. In addition, the measurements presented in this work are surface sensitive. Especially at low photon energies, the x-ray attenuation length in the MgO cap layer and the $Fe_3Si$ is reduced to about 10 nm.[40] Therefore, even a thin Si-enriched layer at the surface of $Fe_3Si$ may strongly affect the XANES. However, the contribution of c-FeSi or other Fe-Si compounds to the XMCD is negligible since they do not exhibit any ferromagnetic order. Thus, the Si atoms near the surface will not measurably contribute to the XMCD asymmetry if the composition significantly deviates in this region. The XMCD signal compared to the XANES intensity would be reduced as a consequence. Note that a difference in the intensities of the double-peak structure for annealed and nonannealed samples could not be obtained. The annealing appears not to change the composition along the depth if we follow the arguments above.

At higher photon energies, e.g., at the Si K edge, the measurement is less surface sensitive and the contribution of the bulk of $Fe_3Si$ to the total signal is larger. However, the TEY detection mode of XANES and XMCD still leads to an emphasis of the signal arising from surface atoms due to self-absorption effects. Therefore, it is also reasonable to scale experimental XANES and XMCD with different factors for comparison to theory.

From computational aspects, there is also a distinct uncertainty in the amplitude of XANES because of the exclusion of final state effects as mentioned before. Better quality of comparison for the XMCD spectra is due to cancellation of this effect yielding different scaling factors for XANES and XMCD to match experimental data. In addition, it seems to be a general trend in such alloys, that theory underestimates the orbital contributions to the total magnetic moments and often overestimates spin moments whereby the overestimation of the spin moments is produced by the GGA and the small orbital moments are related to correlation effects. All these effects discussed here are reflected in the large error bars of the magnetic moments estimated from the experimental data.

## V. CONCLUSION

In summary, we were able to detect the XMCD signal at both the Si $L_{3,2}$ and Si K absorption edge respectively for highly ordered $Fe_3Si$ films on a MgO tunnel barrier. Orbital and spin magnetic moments are aligned antiparallel to the magnetic moments of Fe and could be quantified by comparison to calculated spectra. While the spin magnetic moment of Si $\mu_s^{\text{eff}} = (-0.011 \pm 0.005)\ \mu_B$ is estimated to be smaller than predicted by theory, the orbital magnetic moment $\mu_l = (-0.003 \pm 0.003)\ \mu_B$ is about twice as large as the theoretically expected value. Both reduced spin and enhanced orbital magnetic moment may be explained by the surface sensitivity of the TEY mode employed in this work, a possible Si-enrichment in the surface layer of $Fe_3Si$, and uncertainties in the calculated XANES amplitudes.

In addition, the field dependence of the XMCD at the Si K edge as a measure of the change of orbital magnetization with the applied external magnetic field could be obtained. Our findings demonstrate the possibility to detect extremely weak induced magnetic moments and use them for the determination

of local atomic structures through synergistic theoretical and experimental work.

## ACKNOWLEDGMENTS

We would like to thank P. Wulkow (U. Duisburg-Essen) for help in the measurements and the HZB BESSY II staff, especially H. Pfau and R. Schulz for their kind support. Funded by BMBF (05 ES3XBA/5) and DFG (SFB 491). Work in the UCI was supported by US-DOE grant DE-FG02-05ER46237. Calculations were performed on parallel computers at NERSC. J.L. thanks the Alexander von Humboldt Foundation for support through the Feodor Lynen program.

[1] A. T. Hanbicki, B. T. Jonker, G. Itskos, G. Kioseoglu, and A. Petrou, Appl. Phys. Lett. **80**, 1240 (2002).
[2] G. Schmidt and L. W. Molenkamp, Semicond. Sci. Technol. **17**, 310 (2002).
[3] S. Hövel, N. C. Gerhardt, M. R. Hofmann, F.-Y. Lo, A. Ludwig, D. Reuter, A. D. Wieck, E. Schuster, H. Wende, W. Keune, O. Petracic, and K. Westerholt, Appl. Phys. Lett. **93**, 021117 (2008).
[4] A. Kawaharazuka, M. Ramsteiner, J. Herfort, H.-P. Schönherr, H. Kostial, and K. H. Ploog, Appl. Phys. Lett. **85**, 3492 (2004).
[5] M. Stearns, Phys. Rev. **129**, 1136 (1963); A. Paoletti and L. Passari, Nuovo Cimento **32**, 25 (1964); M. B. Stearns, Phys. Rev. B **4**, 4069 (1971).
[6] M. Arita, S. Nasu, and F. E. Fujita, Trans. Jpn. Inst. Met. **26**, 710 (1985).
[7] G. Vogl and M. Hartmann, J. Phys.: Condens. Matter **13**, 7763 (2001).
[8] B. Krumme, C. Weis, H. C. Herper, F. Stromberg, C. Antoniak, A. Warland, E. Schuster, P. Srivastava, M. Walterfang, K. Fauth, J. Minár, H. Ebert, P. Entel, W. Keune, and H. Wende, Phys. Rev. B **80**, 144403 (2009).
[9] G. Schmidt, D. Ferrand, L. W. Molenkamp, A. T. Filip, and B. J. van Wees, Phys. Rev. B **62**, R4790 (2000).
[10] E. G. Moroni, W. Wolf, J. Hafner, and R. Podloucky, Phys. Rev. B **59**, 12860 (1999).
[11] R. Kläsges, C. Carbone, W. Eberhardt, C. Pampuch, O. Rader, T. Kachel, and W. Gudat, Phys. Rev. B **56**, 10801 (1997).
[12] J. D. Jackson, *Classical Electrodynamics* (Wiley, New York, 1998).
[13] B. T. Thole, P. Carra, F. Sette, and G. van der Laan, Phys. Rev. Lett. **68**, 1943 (1992).
[14] P. Carra, B. T. Thole, M. Altarelli, and X. Wang, Phys. Rev. Lett. **70**, 694 (1993).
[15] C. T. Chen, Y. U. Idzerda, H.-J. Lin, N. V. Smith, G. Meigs, E. Chaban, G. H. Ho, E. Pellegrin, and F. Sette, Phys. Rev. Lett. **75**, 152 (1995).
[16] J. I. Igarashi and K. Hirai, Phys. Rev. B **50**, 17820 (1994).
[17] J. I. Igarashi and K. Hirai, Phys. Rev. B **53**, 6442 (1996).
[18] R. Nakajima, J. Stöhr, and Y. U. Idzerda, Phys. Rev. B **59**, 6421 (1999).
[19] E. Goering, A. Fuss, W. Weber, J. Will, and G. Schütz, J. Appl. Phys. **88**, 5920 (2000).
[20] C. S. Wang and J. Callaway, Phys. Rev. B **9**, 4897 (1974).
[21] H. Ebert *et al.*, The Munich SPR-KKR package, version 3.6, [http://olymp.cup.uni-muenchen.de/ak/ebert/SPRKKR]; H. Ebert, in *Fully Relativistic Band Structure Calculations for Magnetic Solids – Formalism and Application* in *Electronic Structure and Physical Properties of Solids*, edited by H. Dreyssé, Lecture Notes in Physics, Vol. 535 (Springer Berlin, 2000) p. 191.
[22] E. Wimmer, H. Krakauer, M. Weinert, and A. J. Freeman, Phys. Rev. B **24**, 864 (1981).
[23] M. Weinert, E. Wimmer, and A. J. Freeman, Phys. Rev. B **26**, 4571 (1982).
[24] R. Q. Wu and A. J. Freeman, J. Magn. Magn. Mater. **200**, 498 (1999).
[25] J. P. Perdew, Phys. Rev. B **33**, 8822 (1986).
[26] J. P. Perdew, K. Burke, and M. Ernzerhof, Phys. Rev. Lett. **77**, 3865 (1996).
[27] M. Asato, A. Settels, T. Hoshino, T. Asada, S. Blügel, R. Zeller, and P. H. Dederichs, Phys. Rev. B **60**, 5202 (1999).
[28] V. Ozoliņš and M. Körling, Phys. Rev. B **48**, 18304 (1993).
[29] F. Lechermann, F. Welsch, C. Elsässer, C. Ederer, M. Fähnle, J. M. Sanchez, and B. Meyer, Phys. Rev. B **65**, 132104 (2002).
[30] D. J. Singh and J. Ashkenazi, Phys. Rev. B **46**, 11570 (1992).
[31] J. J. Rehr and R. C. Albers, Rev. Mod. Phys. **72**, 621 (2000).
[32] Nan Jiang, Mater. Res. Soc. Symp. Proc. **1152**, TT01 (2011).
[33] R. Q. Wu, Phys. Rev. Lett. **94**, 207201 (2005).
[34] V. N. Antonov, A. N. Yaresko, and O. Jepsen, Phys. Rev. B **81**, 075209 (2010).
[35] H. Chen, W. Zhu, E. Kaxiras, and Z. Zhang, Phys. Rev. B **79**, 235202 (2009).
[36] T. Huhne, C. Zecha, H. Ebert, P. H. Dederichs, and R. Zeller, Phys. Rev. B **58**, 10236 (1998).
[37] H. Wende, Rep. Prog. Phys. **67**, 2105 (2004).
[38] U. Starke, J. Schardt, W. Weiss, W. Meier, C. Polop, P. L. de Andres, and K. Heinz, Europhys. Lett. **56**, 822 (2001).
[39] M. Vondráček, V. Dudr, N. Tsud, P. Lejček, V. Cháb, K. C. Prince, V. Matolín, and O. Schneeweiss, Surf. Sci. **600**, 4108 (2006).
[40] B. L. Henke, E. M. Gullikson, and J. C. Davis, At. Data Nucl. Data Tables **54**, 181 (1993), [http://henke.lbl.gov/optical_constants/].